Orbital effect, subband depopulation, and conductance fluctuations in ballistic quantum dots under a tilted magnetic field

C. Gustin,[1,*] S. Faniel,[1] B. Hackens,[1] S. Melinte,[1] M. Shayegan,[2] and V. Bayot[1]
[1]*CERMIN, PCPM, and DICE Laboratories, Université Catholique de Louvain, B-1348 Louvain-la-Neuve, Belgium*
[2]*Department of Electrical Engineering, Princeton University, Princeton, New Jersey 08544, USA*
(Received 25 October 2004; published 15 April 2005)

Using two-dimensional electron gases (2DEGs) confined to wide and narrow quantum wells, we study the magnetoconductance of ballistic quantum dots as a function of the well width and the tilt angle of the magnetic field B with respect to the 2DEG. Both the wide and narrow quantum well dots feature magnetoconductance fluctuations (MCFs) at intermediate tilt angles, due to the finite thickness of the electron layer and the field-induced orbital effect. As B approaches a strictly parallel configuration, a saturation of the MCFs' spectral distribution is observed, combined with the persistence of a limited number of frequency components in the case of the narrow quantum well dot. It is found that the onset of saturation strongly depends on the width of the confining well. Using the results of self-consistent Poisson-Schrödinger simulations, the magnetoconductance is rescaled as a function of the Fermi level in the 2DEG. We perform a power spectrum analysis of the parallel field-induced MCFs in the energy space and find a good agreement with theoretical predictions.

DOI: 10.1103/PhysRevB.71.155314 PACS number(s): 73.63.Kv, 73.63.Hs, 73.23.Ad

I. INTRODUCTION

Quantum dots patterned on top of two-dimensional electron gases (2DEGs) are now commonly used as an experimental tool for the investigation of a particular regime of quantum transport where the electron dynamics is both ballistic and coherent. In particular, the magnetoconductance fluctuations (MCFs) observed in ballistic quantum dots have been the subject of intensive research[1–4] in the last few years. The fluctuations arise from the complex quantum interferences occurring between electron trajectories that bounce multiple times against the dot walls before escaping through its leads. Unlike disordered systems where transport is essentially chaotic, the underlying classical dynamics in open quantum dots is characterized by a mixed (chaotic and regular) phase space[5] with quantum-mechanical tunneling of the electrons through Kolmogorov-Arnol'd-Moser (KAM) islands.[6] Central to quantum interference phenomena is the presence of a magnetic field that breaks the time-reversal symmetry and changes the phase experienced by electrons in the dot.[7]

Until recently, the magnetic field B was usually applied perpendicular to the 2DEG in order to maximize the magnetic flux enclosed by electron trajectories. Seminal experiments and theoretical works[8,9] have shown that the presence of a component of the field parallel to the 2DEG can strongly affect the MCFs' statistics, mainly due to the spin-orbit coupling, which is non-negligible in GaAs quantum dots.[10,11] Other authors have focused their attention[12–15] on the complementary role that the orbital effect could play in parallel B-induced transport through quantum dots when the finite thickness of the 2DEG is taken into account. In a recent publication,[16] we showed that MCFs can indeed be observed for ballistic quantum dots under a strictly parallel B. A careful analysis of their variance confirmed that the MCFs arise from the orbital effect.

The use of tilted fields has already proved successful in the study of various quantum Hall states displayed by the 2DEGs at low temperatures and in the presence of a high B.[17,18] In the case of ballistic quantum dots, tilted-field magnetotransport is potentially interesting as it might shed light on the (dis-)similarities between the phase spaces probed by either a perpendicular or parallel field and on the role played by the finite thickness of the 2DEG.[19,20]

Here, we have investigated two ballistic quantum dots patterned on top of 2DEGs confined to a narrow and a wide quantum well, respectively. We have studied their magnetoconductance as a function of the well width and the tilt angle θ of the magnetic field B with respect to the normal to the 2DEG. The plan of the paper and the main results of our work are as follows. In Sec. II, we present our magnetotransport results. After a brief description of the experimental details, the measurements related to the narrow quantum well (NQW) dot are described in Sec. II A and are followed by their counterparts in the case of the wide quantum well (WQW) dot in Sec. II B. In both NQW and WQW dots a rich spectrum of MCFs is present when B is brought to a strictly parallel configuration ($\theta=90°$), due to the finite thickness of the electron layer and the orbital effect it induces. In Sec. III, we analyze the MCFs' power spectrum in tilted magnetic fields and extract an effective tilt angle, which is a useful parameter to analyze the dependence on the well width of the MCFs' fingerprint. Section IV is devoted to self-consistent Poisson-Schrödinger calculations of the two-dimensional electronic states under a parallel field,[21,22] in both narrow and wide QWs. Particular emphasis is put on the influence of the orbital effect on the energy dispersion relations, Fermi level contours, and electron concentrations in the occupied subbands. Our data analysis is presented in Sec. V. We introduce a remapping of B into a self-consistently calculated effective Fermi energy in the QWs. The frequency analysis of the MCFs in the *energy space* is in good agreement with theoretical predictions.[23] We draw our conclusions in Sec. VI.

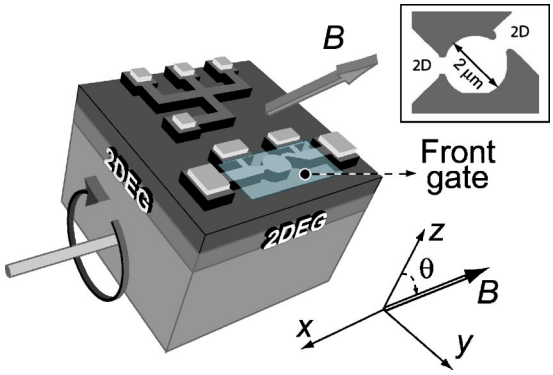

FIG. 1. Schematic of the experimental setup with *in situ* tilting of the sample. The tilt angle θ is determined by monitoring the 2DEG transverse magnetoresistance in the Hall bar located next to the dot. Upper inset: Schematic diagram of the dot. Dark regions represent etched areas of the 2DEG. The dot is connected to 2D reservoirs through two quantum point contacts.

II. EXPERIMENT

Two identical dots with an area of 3 μm^2 have been fabricated using electron beam lithography and wet etching from two 2DEGs (see Fig. 1). The first 2DEG is confined to a 15-nm-thick quantum well (NQW), located 100 nm below the surface. This NQW sample has a mobility $\mu \sim 5\times10^5$ cm^2/V s. The second 2DEG is confined to a 45 -nm-thick quantum well. This WQW is located 150 nm below the surface and its mobility is $\mu \sim 1.6\times10^6$ cm^2/V s. Because of the difference in thickness between the two QWs, one and two transversal subbands are populated by electrons at $B=0$ in the NQW and WQW, respectively, as confirmed by standard Shubnikov–de Haas measurements (Fig. 2). A Cr/Au electrostatic gate, deposited on top of both the dot and its measuring voltage leads, is used as a means to control the width of the dot openings (Fig. 1). Throughout the measurements, a constant gate voltage V_F of −0.25 and 0.65 V is applied for the NQW and WQW dots, respectively. The densities of the 2DEGs are $n_s=2.2\times10^{11}$ cm^{-2} (NQW) and $n_s=3.2\times10^{11}$ cm^{-2} (WQW). The positive potential applied for the WQW dot was required in order to have at least one transmission mode in each of the two quantum point contacts connecting the otherwise closed dot at $V_F=0$ to the electron reservoirs. Rough estimates of the mean free path based on the mobilities and subband densities in our samples[52] give values of 4 μm in the NQW, 9 and 12 μm for the upper and lower subbands in the WQW, respectively—larger than the lateral dimensions of the dots. The two dots were characterized in a He-3 cryostat with a base temperature $T=0.3$ K after having been cooled down in the dark. A standard, 4-contact low-frequency lock-in technique was used to measure their conductance with a current of 1 nA.

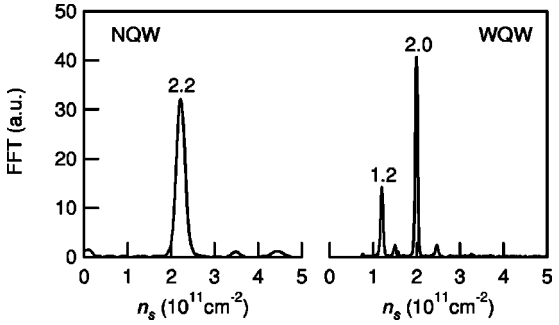

FIG. 2. Fast Fourier transform (FFT) of Shubnikov–de Haas oscillations for the NQW and WQW. The positions of the FFT peaks correspond to the subband densities.

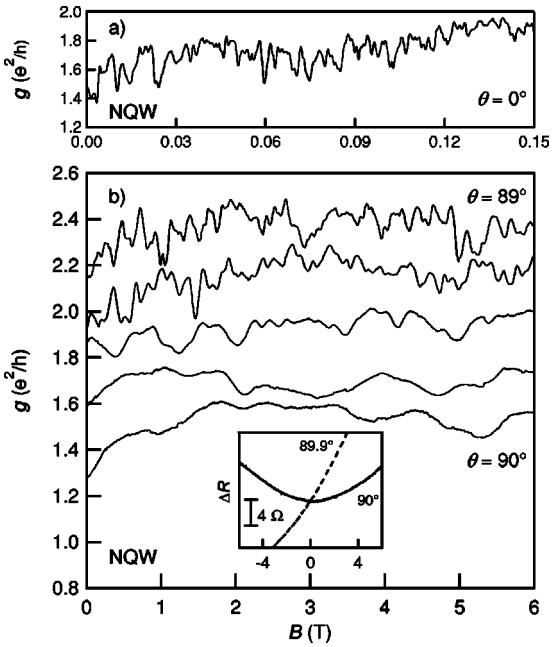

FIG. 3. (a) Magnetoconductance g of the NQW dot at $T=0.3$ K under a strictly perpendicular B. (b) Magnetoconductance of the NQW dot for tilt angles close to 90° (θ=89°, 89.3°, 89.6°, 89.9°, and 90° from the upper to the lower curve). The traces are shifted for clarity in steps of $0.2e^2/h$ with respect to the θ=90° curve. Inset: Transverse resistance of the parent 2DEG at indicated tilt angles, measured on the adjacent Hall bar (see Fig. 1).

The samples are mounted on a sample holder that can be tilted *in situ* with respect to the magnetic field. The tilt angle is precisely controlled by monitoring the transverse magnetoresistance $R_{xy}(\theta,B)$ of the 2DEG on a Hall bar located on the same wafer, 300 μm away from the dot (Fig. 1). The value of the tilt angle θ is extracted from the ratio of the slopes of $R_{xy}(\theta,B)$ and $R_{xy}(0,B)$ with respect to B. The precision improves with increasing θ and reaches a value of 0.01° in the configuration where B is parallel to the 2DEG.

A. Narrow quantum well

Figure 3(a) shows the results of a typical magnetoconductance measurement performed at $T=0.3$ K on the NQW dot under a perpendicular magnetic field only. Reproducible MCFs with no clear periodic pattern are superimposed upon a slowly varying background. The investigated B range is limited to 0.15 T in order to avoid the coexistence of both interference-induced fluctuations and Shubnikov–de Haas oscillations that appear at higher magnetic fields when the cyclotron radius becomes commensurate with the dot size.

As a next step, the magnetic field was tilted away from its perpendicular configuration and the magnetoconductance was measured at various θ's as shown in Fig. 3(b). We point out that the curves are presented as a function of the *total* magnetic field. For $\theta \geqslant 89°$, the conductance fluctuations first shift to lower frequencies ($\theta = 89.3$ and $89.6°$), as expected for perpendicular B-induced MCFs, but saturate at $\theta = 89.9°$. While the $\theta = 89.9°$ and $90°$ traces are not identical, they definitively share common features, like their major frequency components. The inset to Fig. 3(b) shows the transverse resistance measured on the adjacent Hall bar at these two tilt angles. A strictly parallel B corresponds to a symmetric, quasiparabolic B dependence of the resistance.[53] The difference between the $\theta = 89.9°$ and $90°$ curves demonstrates the precision achieved with the experimental setup and confirms that the MCFs at $\theta = 90°$ cannot be attributed to a residual perpendicular component of the field. However, one needs to confirm that the low-frequency oscillations observed under a parallel B cannot be linked to a ballistic effect[24,25] across the open dot but, instead, are generated by interference effects between electron trajectories.

To achieve this goal, we investigated the T dependence of the magnetoconductance fluctuations. The strength of the fluctuations as a function of temperature is indeed a good indication of their origin. The electron mean free path, the key player in electron focusing,[26,27] is much less sensitive to temperature than the phase relaxation length that limits the MCFs' amplitude.[28] Figure 4(a) shows the temperature dependence of the fluctuations amplitude $\delta g(B) = g(B) - g^{\star}(B)$ in the NQW dot under a perpendicular B only. Here $g^{\star}(B)$ is the average, slowly varying, low-frequency background magnetoconductance that remains at high temperature ($T \geqslant 2.5$ K). Upon inspection of Fig. 4(a), it is clear that $\delta g(B)$ rapidly decreases with temperature. This behavior points toward interference effects as the source of the fluctuations. More quantitatively, the MCFs' amplitude, expressed for the NQW sample in terms of its standard deviation $\sigma(g)$, is reduced from $0.076e^2/h$ at $T = 0.3$ K to $0.002e^2/h$ at $T = 2.1$ K [Fig. 5(a), $\diamond$] and follows a $T^{-0.6}$ law. The T dependence of fluctuations generated by a strictly parallel magnetic field in the NQW dot is presented in Fig. 4(b). Clearly visible at $T = 0.3$ K are the relatively low frequency, almost periodic fluctuations superimposed upon a slowly varying background. As the temperature is increased, the fluctuations start to disappear, leaving only the slowly varying background magnetoconductance at $T = 2.8$ K. Because of the small number of fluctuation periods observed at $\theta = 90°$ and their limited frequency distribution compared to their perpendicular B-generated counterparts, it is impossible to extract the standard deviation of the fluctuations. Therefore, the discussion must be limited to a simple analysis of the amplitude reduction of a few oscillations on a selected B range [Fig. 4(b), gray area], where the peak-to-peak amplitude decreases from 0.12 to $0.02e^2/h$ between $T = 0.3$ and 2.8 K. The four data points are illustrated in Fig. 5(a) (■). The best power law fit gives a $T^{-0.8}$ temperature dependence, close to the $T^{-0.6}$ law observed for the perpendicular B-induced MCFs. Even though this comparison is not fully conclusive, it nevertheless seems reasonable to give a common electron coherence origin to these similar reductions of the MCFs' amplitude under both a perpendicular and parallel B.

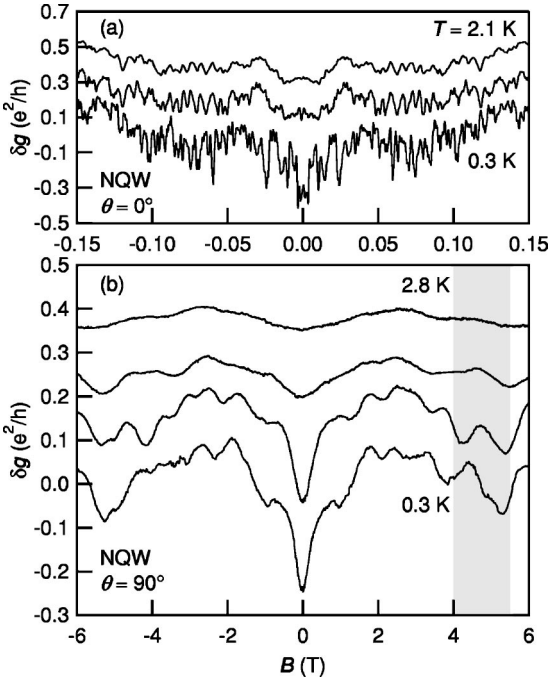

FIG. 4. (a) T dependence of the NQW dot magnetoconductance under a strictly *perpendicular B*. The temperatures are 2.1, 1.1, and 0.3 K from top to bottom. (b) The temperature dependence of the NQW dot magnetoconductance under a strictly *parallel B*. The temperatures are 2.8, 1.5, 0.8, and 0.3 K from top to bottom, respectively. The gray area indicates the B range for which the MCFs' peak-to-peak amplitude is determined (see the text). The traces in panels (a) and (b) are shifted in steps of $0.1e^2/h$ with respect to the $T = 0.3$ K curves.

We close this section with a discussion of the dephasing time τ_φ in the perpendicular magnetic field configuration. Using an expression[29] valid for interference-induced MCFs, τ_φ can be extracted from the variance of the conductance fluctuations using the generalized formula

$$\mathrm{var}(g) = \langle \delta g^2 \rangle - \langle \delta g \rangle^2 = \sigma^2(g) = \int_0^\infty \int_0^\infty f'(E) f'(E') C(E,E') dE\, dE', \qquad (1)$$

where f' is the first derivative of the Fermi distribution. Here $C(E,E') = \langle g \rangle^2 / [(N+N_\varphi)^2 + 4\pi (E-E')^2/\Delta^2]$ is the conductance correlator, $\Delta = 2\pi\hbar^2/Am^*$ the mean level spacing, m^* the electron effective mass, $\langle g \rangle$ is the average conductance, A the dot area, and $N_\varphi = 2\pi\hbar/(\tau_\varphi \Delta)$ and N are the number of dephasing channels and of transmission modes in the dot openings, respectively. A thermal average was explicitly included as the mean level spacing is not negligible with respect to the thermal energy [$\Delta/(kT) \simeq 0.1$ at $T = 0.3$ K]. The value of τ_φ calculated from Eq. (1) and shown in Fig. 5(b) follows a $T^{-1.2}$ power law, consistent with results from the literature.[30,31] The corresponding number of dephasing channels N_φ increases from 5 to 20 in the same temperature

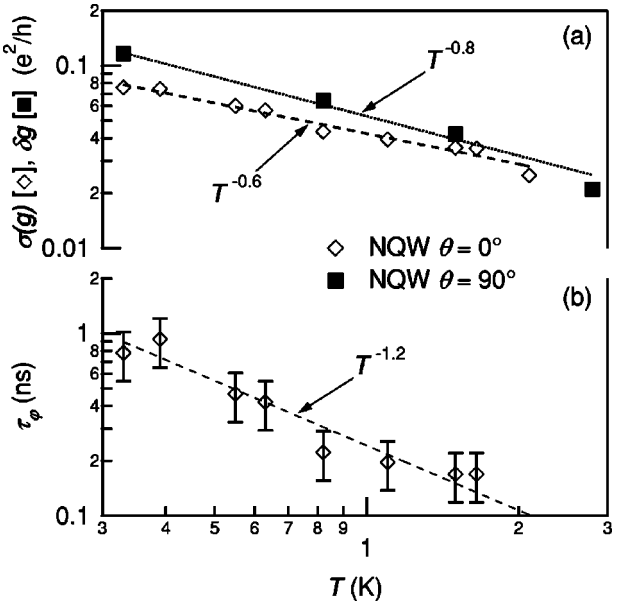

FIG. 5. (a) MCFs amplitude vs T at $\theta=0°$ (standard deviation, ◇) and $\theta=90°$ (peak to peak, ■) in the NQW. The dashed curves are two-parameter power law fits to data points. (b) T dependence of the dephasing time τ_φ extracted from Eq. (1) for the MCFs at $\theta=0°$ in the NQW.

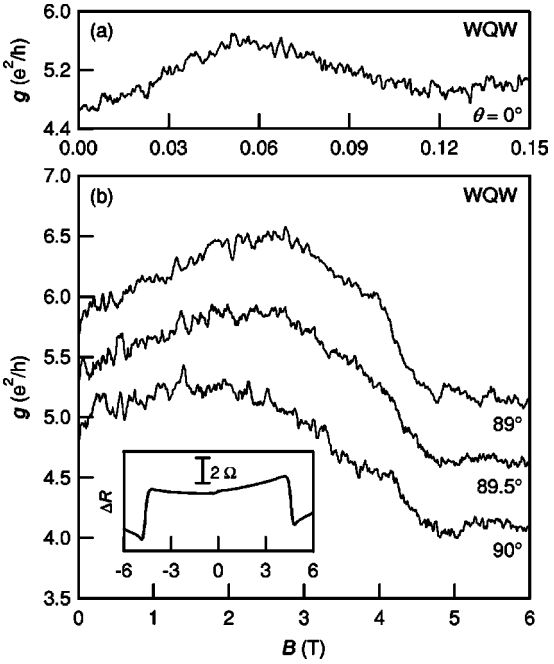

FIG. 6. (a) Low-temperature magnetoconductance of the WQW dot under a strictly perpendicular B. (b) Magnetoconductance of the WQW dot at indicated tilt angles. The traces are shifted in steps of $0.5e^2/h$ with respect to the $\theta=90°$ magnetoconductance curve. Inset: Transverse magnetoresistance of the 2DEG measured on the adjacent Hall bar (see Fig. 1). Note the parabolic-like variation of ΔR already present for the NQW dot on the transverse magnetoresistance of Fig. 3(c) and the step around 4.2 T.

range. At base T, N_φ is thus close to the number of transmission modes in the dot openings ($N \simeq 3$ for $\langle g \rangle \simeq 1.5e^2/h$).

B. Wide quantum well

We now focus our attention on the WQW sample. Figure 6(a) shows the magnetoconductance of the WQW dot under a strictly perpendicular B at $T=0.3$ K. The average conductance $\langle g \rangle$ across the dot is $5.2e^2/h$. Apart from the difference in the shape of the background magnetoconductance, the MCFs' fingerprint is similar to the fluctuations observed at $\theta=0°$ in the NQW dot [Fig. 3(a)]. The MCFs' variance is constant over the investigated B range [$\mathrm{var}(g)=3.4 \times 10^{-3}\ e^4/h^2$] and $N_\varphi \simeq 27$. As stated earlier in the text, N_φ in the fictitious voltage probe model[32] depends only upon the dephasing time τ_φ and the mean-level spacing Δ, which is constant in the NQW and WQW dots because of their identical shape and area. The larger N_φ observed for the WQW dot is thus caused by an increased dephasing that can have several origins:[33,34] a higher electron-electron scattering rate and Nyquist dephasing. However, in the WQW dot, we speculate that the increased dephasing, resulting in a large N_φ, originates from inter-subband scattering,[35] due to the presence of two occupied subbands in the WQW, and from a greater sensitivity of the WQW sample to both switching noise and external radiations.

After the $\theta=0°$ measurements, the sample is tilted in the magnetic field. Magnetoconductances at high θ's, including $\theta=90°$, are shown in Fig. 6(b). Note that the magnetoconductance traces illustrated in this figure are expressed in terms of the *total* magnetic field. Comparing these curves to their counterparts obtained for the NQW dot [Fig. 3(b)], three main characteristics can be pointed out. First, the MCFs have a much richer frequency spectrum, i.e., higher frequency components are present in the WQW dot. Second, this frequency distribution of the MCFs is not significantly modified as the sample is slightly tilted away from the 90° position. If the MCFs had their origin in the perpendicular component of the field, one would expect a progressive shift of the fluctuations toward lower frequencies with increasing tilt angle. Although this shift occurs for the NQW dot in Fig. 3, this is not the case with the WQW dot. This observation suggests that the finite width of the QW plays a significant role for the parallel B-induced MCFs and it reveals the importance of tilted magnetic field magnetotransport studies. The third difference concerns the magnetoconductance at $\theta=90°$. We observe in the WQW dot a sudden drop in $\langle g \rangle$ that occurs around $B=4.2$ T. In contrast, the magnetoconductance in the NQW dot fluctuates over the entire B range around its average value determined by the dot openings. In a previous study,[16] this reduction of $\langle g \rangle$ in the WQW dot was attributed to the magnetic subband depopulation of the upper electronic subband and the corresponding reduction of the number of transmission modes in the dot openings.[36] This conjecture is further supported by the inset to Fig. 6(b), where the transverse magnetoresistance of the unpatterned 2DEG is measured on the adjacent Hall bar. The sharp drop in the resistance[37] near $B=4.2$ T gives a good measure of the magnetic field where the upper subband becomes fully depleted, as it corresponds to a reduction of intersubband scattering.

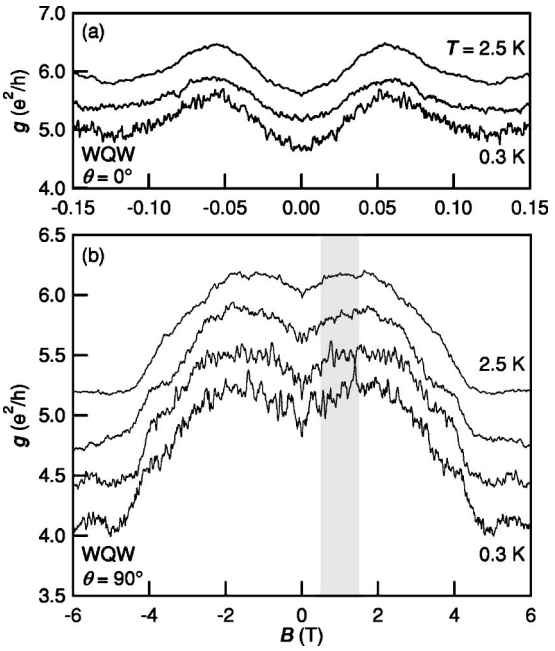

FIG. 7. (a) Temperature dependence of the WQW dot magnetoconductance under a strictly *perpendicular B*. The temperatures are 2.5, 1.5, and 0.3 K from top to bottom. (b) The magnetoconductance curve of the WQW dot under a strictly *parallel B* at various *T*'s. From the upper to the lower curve, the temperatures are 0.3, 0.6, 1.5, and 2.5 K, respectively. The gray area indicates the *B* range for which the fluctuation's amplitude is determined (see the text). The traces in panels (a) and (b) are shifted in steps of $0.4e^2/h$ with respect to the $T=0.3$ K magnetoconductance curves.

The temperature dependence of the WQW dot magnetoconductance under a strictly perpendicular and parallel *B* is shown in Fig. 7. The curves are presented here in a symmetric *B* range. The *T* dependence observed in the WQW dot looks similar to that found for the NQW dot (Fig. 4). The most important feature is that the MCF's amplitude is reduced with increasing temperature and the oscillations are barely visible at $T=2.5$ K. Following the same procedure used for the $\theta=0°$ magnetoconductance in the NQW dot, it is possible to obtain an estimate of τ_φ for the $\theta=0°$ MCFs in the WQW dot. It is found that τ_φ decreases with the temperature according to a $T^{-0.8}$ power law (Fig. 8, △). This is slightly lower than the $T^{-1.2}$ dependence of the $\theta=0°$ fluctuations observed in the NQW dot (Fig. 5), a result of the greater dephasing taking place in the WQW dot and already mentioned earlier in the text.

The reduction of MCFs amplitude with increasing parallel magnetic field, clearly visible on the $T=0.3$ K trace of Fig. 4(b) has been discussed in a previous publication.[16] In particular, this reduction was attributed to the complementary role played by the *B*-induced subband depopulation and time-reversal symmetry breaking.[12–14] Precisely because the MCFs amplitude is not constant with *B*, a quantitative analysis using Eq. (1) has to be performed in a small *B* range, as opposed to the $\theta=0°$ fluctuations where the full *B* range can be used. For the gray area displayed in Fig. 7, the standard deviation of MCFs amplitude decreases from 0.066 to $0.013e^2/h$ between 0.3 and 2.5 K. The corresponding dephasing time τ_φ follows a $T^{-0.8}$ power law (Fig. 8, ●). This behavior is consistent with the amplitude reduction of parallel *B*-induced fluctuations observed in the NQW dot [Fig. 5(a)]. The similar *T* dependencies for the fluctuations observed at $\theta=90°$ in the NQW and WQW dots confirm that they have a common origin, i.e., coherent interference effects as opposed to focusing.

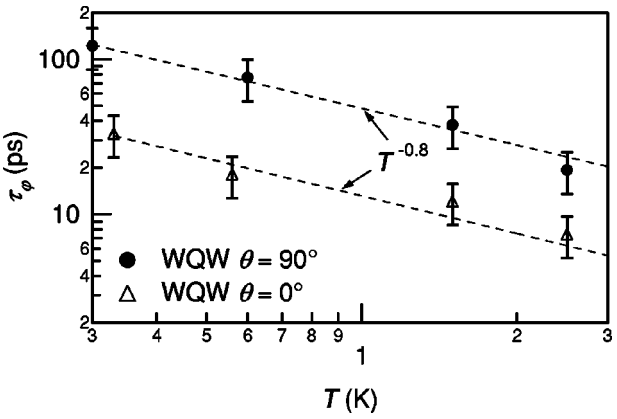

FIG. 8. *T* dependence of the dephasing time τ_φ extracted from Eq. (1) for the $\theta=0°$ (△) and $\theta=90°$ (●) MCFs in the WQW. The dashed lines are two-parameter power law fits to the data points.

Figure 9 summarizes the main results obtained when the NQW (upper row) and WQW (lower row) dots are subject to a strictly perpendicular (left column) and parallel (right column) magnetic field. For all the traces, the corresponding, temperature-independent background was subtracted, leaving only the fluctuations induced by electron coherent effects. The three important observations are as follows: the presence of MCFs in a strictly parallel field [panels (b) and (d)], the difference in the MCFs' frequency distribution between the NQW and WQW dot (all panels), and the reduction of the

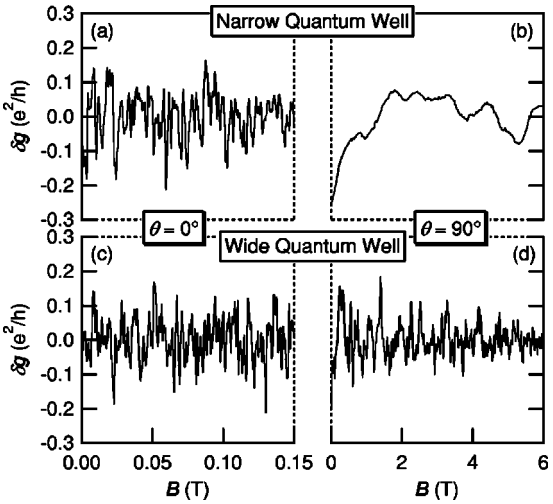

FIG. 9. MCFs of the NQW (upper row) and WQW (lower row) under a strictly perpendicular (left column) and parallel (right column) *B*. To isolate the MCFs, a slowly varying background corresponding to the high-*T* magnetoconductances (Figs. 4 and 7) was removed from the raw curves of Figs. 3 and 6, at the corresponding tilt angles.

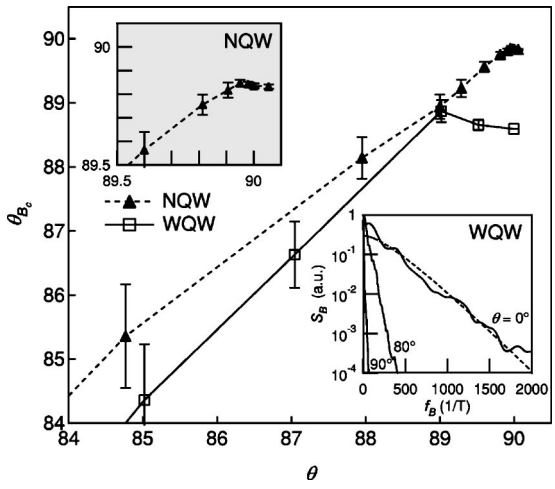

FIG. 10. The effective tilt angle θ_{B_c} calculated from the correlation field B_c (see the text) is shown as a function of the angle θ extracted from Hall measurements. Here θ_{B_c} is calculated for $\theta \geqslant 84°$ for both the WQW (□) and NQW (▲) dots. The plain and dotted curves are a guide to the eye. Upper inset: Zoom into the $\theta \geqslant 89.5°$ range for the NQW dot. Lower inset: Power spectra of the WQW dot MCFs for $\theta = 0°$, 89°, and 90°. The dashed curve is a fit to the $\theta = 0°$ data (see the text).

MCFs amplitude with increasing B for the strictly parallel field configuration in the WQW dot [panel (d)].

III. MCFs' FREQUENCY ANALYSIS

We now turn to the frequency distribution of both the NQW and WQW MCFs as a function of the tilt angle θ. From the comparison of Figs. 3(b) and 6(b), it is clear that the two dots react differently to the presence of a tilted B. To quantitatively analyze the role played by the parallel component of the field on the production of MCFs, compared to the fluctuations solely attributed to the perpendicular component of B, we evaluate the power spectrum of the magnetoconductance curves at tilt angles close to $\theta = 90°$. This method is commonly used for the determination of the temperature-dependent dephasing time[28] or to study shape-induced fluctuations[38] in open quantum dots. In our sample, the autocorrelation function of the conductance fluctuations with respect to the magnetic field is Lorentzian-squared[39] and the corresponding MCFs power spectrum reads as

$$S_B(f_B) = S_B(0)[1 + 2\pi B_c f_B]e^{-2\pi B_c f_B}, \tag{2}$$

where f_B is the frequency in $[1/\mathrm{T}]$ and B_c is a correlation field. For each magnetoconductance curve at a tilt angle θ, $S_B(f_B)$ is first evaluated with $\delta g(B)$ expressed in terms of the *total* magnetic field. The correlation field $B_c(\theta)$ is then calculated by fitting the experimental power spectrum with Eq. (2). An effective tilt angle $\theta_{B_c}(\theta)$ is subsequently extracted from $B_c(\theta)$ using the expression

$$B_c(\theta) = B_c(\theta = 0)/|\cos\,\theta_{B_c}|. \tag{3}$$

In Fig. 10, values of θ_{B_c} obtained from Eq. (3) for both the NQW and WQW dots are compared to the real tilt angle θ of the sample, extracted from the 2DEG transverse magnetoresistance in the Hall bar located near the dot. Typical MCFs' power spectra at various θ's, along with a fit to Eq. (2) used for the evaluation of θ_{B_c} at $\theta = 0°$, are presented for the WQW dot in the lower inset to Fig. 10. In both the NQW and WQW dots, θ_{B_c} has a linear dependence on θ at low tilt angles but saturates as $\theta \to 90°$. The onset of saturation is observed at $\theta = 89°$ in the WQW dot, compared to $\theta = 89.9°$ in the NQW dot (upper inset to Fig. 10). For MCFs created by a perpendicular B, one would expect a strict linear dependence $\theta_{B_c} \equiv \theta$ at all tilt angles. The observed saturation thus indicates that above some QW-dependent tilt angle (close to 90°), MCFs are generated mainly by the in-plane component of B.

For an ideal, zero-thickness 2DEG, a parallel field should have no effect on electron dynamics in the dots: classically, it induces no Lorentz force that could bend the electron paths, and quantum mechanically it produces no magnetic flux, hence no interferences among trajectories. Therefore, the MCFs that dominate above the saturation angle must have a different origin from the fluctuations generated by the perpendicular field. Since the major difference between the two samples is the width of the QWs, the different values of the saturation angle in the NQW and WQW dots indicate that a parallel field has a stronger effect with respect to the production of MCFs when the 2DEG is weakly confined in the QWs. It is thus natural to invoke the interplay between the electrostatic and magnetic energies as the source of these parallel B-induced MCFs. The value of the saturation angle would then be an indication of the threshold point where the magnetic confinement of the 2DEG becomes commensurate in strength with the electrostatic one.

In order to have a better understanding of the interplay between magnetic and electrostatic confinement of the 2DEG and their combined effect on the production of MCFs by a parallel B, a self-consistent calculation of the energy multiband structure is required and will be the main topic of the next section.

IV. SIMULATIONS

In our previous study,[16] a simple model was introduced to account for the depopulation of electron subbands by a parallel B in the WQW sample. It is indeed well known that the finite thickness of the quantum wells confining the 2DEGs induces an orbital motion of the electrons.[40] Its most important consequence is a modification of the subband energy dispersion relations combined with a diamagnetic shift in reciprocal space of the position of the Fermi energy E_F with respect to the subband minima. Using arguments based on the well width and the onset of upper subband depopulation, a non-negligible quadratic shift of $0.1B^2$ (meV T^{-2}) in B was obtained for the position of E_F in the WQW dot with respect to the bottom of the conduction band. We concluded that a parallel B can play a similar role on E_F as an electrostatic gate, and thus generates MCFs similar to those observed in Fig. 6.

In this section, the interplay between magnetic and electrostatic energy is investigated more quantitatively in terms

of the electronic structure of the 2DEGs confined in the narrow and wide QWs. Our calculations are based on the self-consistent solution of the coupled Schrödinger and Poisson equations. This standard procedure has already been used successfully to study shell-filling effects in quantum dots,[41] in electronic structure calculations of GaAs/AlGaAs heterostructures in a parallel magnetic field,[42] and in explaining the single-to-double layer transitions in bilayer electron systems.[43] Using self-consistent calculations, we precisely determine the conduction energy dispersion relations and the amplitude of the diamagnetic shift. We then perform a remapping of the magnetic field onto a self-consistently calculated effective Fermi energy. The resulting frequency analysis of the MCFs in the energy space is found to be in good agreement with theoretical predictions.[23]

In the case of a 2DEG subjected to a strictly parallel $\mathbf{B}=(0,B,0)$, gauge invariance allows for the choice of a vector potential A with the form $\mathbf{A}=(Bz,0,0)$ where the coordinate system is the one shown in Fig. 1. The Hamiltonian then reads as

$$\hat{\mathcal{H}} = \frac{1}{2m^*}(\mathbf{p} + e\mathbf{A})^2 + E_C(\mathbf{r}) + E_{xc}(\mathbf{r}), \tag{4}$$

where $\mathbf{p}=(p_x,p_y,p_z)=(\hbar k_x,\hbar k_y,p_z)$ is the momentum operator, $E_C(\mathbf{r})$ is the conduction band edge, and E_{xc} is the exchange and correlation energy. The eigenstates Ψ_i solution to the Schrödinger equation $\hat{\mathcal{H}}\Psi_i=\mathcal{E}_i\Psi_i$ can be written as $\Psi_i=\psi_i(k_x,z)e^{-ik_x x}e^{-ik_y y}$ and the corresponding eigenvalues as $\mathcal{E}_i=E_i(k_x)+\hbar^2k_y^2/(2m^*)$. The Schrödinger equation, in its simplified form, becomes $\hat{H}\psi_i(k_x,z)=E_i(k_x)\psi_i(k_x,z)$ with

$$\hat{H} = -\frac{\hbar^2}{2m^*}\frac{\partial^2}{\partial z^2} + \frac{1}{2m^*}(eBz - \hbar k_x)^2 + E_C(z) + E_{xc}(z). \tag{5}$$

The conduction energy $E_C(z)=-e\varphi(z)+\Delta E_{os}$ is the sum of the Hartree energy $[-e\varphi(z)]$ and the conduction band offset ΔE_{os} at the GaAs/AlGaAs interfaces. We obtain the electrostatic potential $\varphi(z)$ by solving the Poisson equation,

$$\frac{\partial}{\partial z}\left(\epsilon(z)\frac{\partial\varphi}{\partial z}\right) = -\rho(z), \tag{6}$$

where $\epsilon(z)$ is the effective permittivity of the material. The charge density $\rho(z)=e[p(z)-n(z)+N_D^+(z)-N_A^-(z)]$ is the signed sum of the hole concentration $p(z)$, electron concentration $n(z)$, and ionized donors and acceptors concentrations $N_D^+(z)$ and $N_A^-(z)$, respectively. For the exchange-correlation energy, we use a local density approximation as parametrized by Ceperley and Alder,[44,45] where E_{xc} can be written as the sum of an exchange E_{ex} and correlation term E_{corr}, functions of the local electron concentration $n(z)$,

$$E_{xc} = -\frac{0.611}{r_s} + \mu_{corr} - \frac{r_s}{3}\frac{d\mu_{corr}(r_s)}{dr_s}, \tag{7}$$

with

$$\mu_{corr}(r_s) = \begin{cases} \dfrac{A}{1 + B\sqrt{r_s} + Cr_s}, & \text{if } r_s \geqslant 1 \\ D + E\ln r_s + Fr_s + Gr_s\ln r_s, & \text{if } r_s < 1, \end{cases} \tag{8}$$

and

$$A = -0.1423, \quad B = 1.0529, \quad C = 0.3334,$$

$$D = -0.0480, \quad E = 0.0311, \quad F = -0.0116, \quad G = 0.0020. \tag{9}$$

In these expressions, r_s is the Seitz radius,

$$r_s = \left[\frac{3}{4\pi n(z)}\right]^{1/3}\frac{1}{a_0^*}, \tag{10}$$

expressed in terms of the effective Bohr radius $a_0^*=\epsilon m_0 a_0/(\epsilon_0 m^*)$, where $\epsilon=13.2\epsilon_0$ is the permittivity of bulk GaAs and a_0 is the Bohr radius. We point out that E_{xc} in Eq. (7) is expressed in scaled atomic units $H_a^*=H_a*(\epsilon_0^2 m^*)/(\epsilon^2 m_0)$, where $H_a=27.2$ eV is the Hartree energy. The hole, ionized acceptors, and donor concentrations are calculated across the entire structure by means of the usual equilibrium charge models for bulk semiconductors.[46] Similarly, in the nonquantized region and in the delta-doping layers, the electron concentration is given by

$$n(z) = 2\left(\frac{k_B T m^*}{2\pi\hbar^2}\right)^{3/2}\mathcal{F}_{1/2}\left(\frac{-E_C(z)}{k_B T}\right), \tag{11}$$

where

$$\mathcal{F}_j(\eta) = \frac{1}{j!}\int_0^{+\infty}\frac{x^j dx}{1+\exp(x-\eta)} \tag{12}$$

is the Fermi-Dirac integral of order j. The electron concentration n in the quantum well is obtained[47] by summing the contributions of the eigenstates $[\psi_i(k_x,z),E_i(k_x)]$, solutions to the Hamiltonian $\hat{H}$ [Eq. (5)],

$$n(z) = \sum_i n_i(z) = \sum_i \sqrt{\frac{2\pi m^* k_B T}{\hbar^2}} \times \frac{1}{2\pi^2}\int_{-\infty}^{+\infty}|\psi_i(k_x,z)|^2\mathcal{F}_{-1/2}\left(-\frac{E_i(k_x)}{k_B T}\right)dk_x. \tag{13}$$

The electronic structure of the 2DEGs is realistically simulated by modeling the GaAs/AlGaAs growth sequence of the NQW and WQW samples. In particular, the position and donor concentrations of the various delta-doping layers are fully taken into account. No assumption is made on the full or partial ionization of the donors. The only parameter left with a degree of freedom is the height of the Schottky barrier ψ_s at the exposed upper surface of the sample. The Dirichlet boundary condition on φ for this region states that the pinning of the Fermi level $[E_C(z=0)-E_F(z=0)]$ is modified to φ_s-V_F by the presence of the electrostatic top gate, where V_F is the gate bias (see Fig. 1). Surface states in GaAs give a

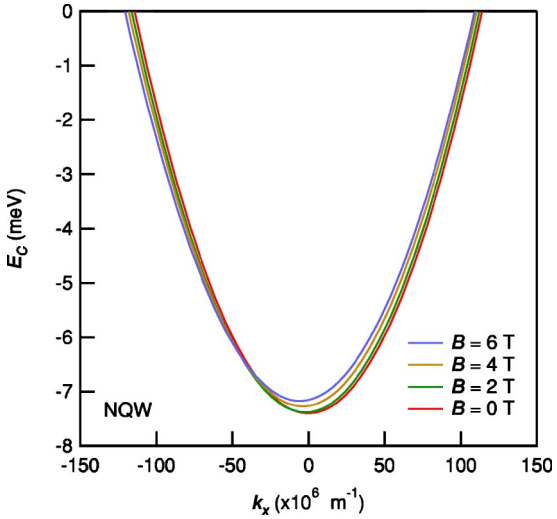

FIG. 11. (Color online) Dispersion relations of the unpatterned 2DEG confined in the NQW sample at indicated values of the parallel B. The 2DEG has a sheet density $n_s=2.2\times10^{11}$ cm^{-2}. The conduction band edge E_C is calculated with respect to the Fermi energy $E_F=0$.

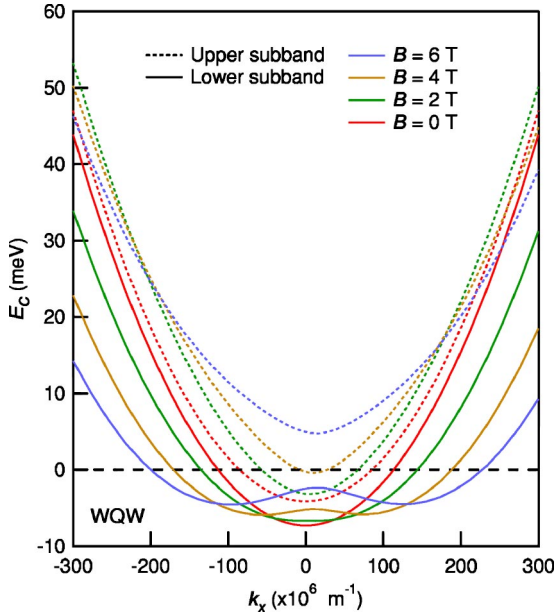

FIG. 12. (Color online) Dispersion relations of the unpatterned 2DEG confined in the WQW sample at indicated values of parallel B. The conduction band edge E_C is calculated with respect to the Fermi energy $E_F=0$. The 2DEG has a sheet density $n_s=3.2\times10^{11}$ cm^{-2} with two occupied subbands at $B=0$. The lower (upper) subband $E_C(k_x)$ relations are represented as plain (dashed) curves.

typical value of ψ_s around 0.8 eV. In our model, ψ_s is slightly adjusted around this target value in order to obtain a perfect agreement between the simulated and experimental 2DEG sheet density n_s for a given range of gate voltages V_F. For the bulk GaAs region at the back of the sample, a von Neumann condition is used for the electrostatic potential φ. It is thus assumed that the electric field vanishes at a distance far enough from the quantum well. For the Schrödinger equation, the eigenfunctions are expected to vanish in the AlGaAs layers surrounding the QWs.

The Schrödinger and Poisson equations are self-consistently solved on the discretized structure. At each self-consistent step, the new solution to the Poisson equation is combined with the solution of a previous iteration using a damping factor on the order of a few percent. Beside its discretization in real space, the Schrödinger equation also requires a division of the reciprocal space. A mesh of 50 values of k_x is required[48] to maintain a constant electron density for all B values. The investigated k_x range is chosen between $-2k_F^0$ and $2k_F^0$, where k_F^0 is the Fermi wave vector calculated at $B=0$.

Figure 11 shows the $E_C(k_x)$ dispersion relation of the conduction band for the NQW as a function of the parallel magnetic field B. The Fermi energy $E_F=0$ is chosen as a reference level. At $B=0$, $E_C(k_x)$ has the expected $\hbar^2k_x^2/(2m^*)$ parabolic profile. When B is increased, the bottom of the conduction is pushed upward in energy and slightly shifted laterally in k-space. This is a result of the increase of the density of states and of the well-known diamagnetic shift. Because the electrostatic confinement in the NQW is quite strong with respect to the magnetic confinement, the dispersion relation is only marginally modified by the parallel B and keeps its parabolic shape even at high fields.

The difference is striking when one compares the NQW results (Fig. 11) to the dispersion relations of the two occupied subbands in the WQW (Fig. 12). Similar to the NQW conduction band, the bottom of the upper subband in the WQW is also lifted in energy with increasing B, but the amplitude of the shift is much larger than with the NQW. Quantitatively, between 0 and 6 T, the energy shift is 9 meV for the upper subband in the WQW but only 0.2 meV in the NQW. As expected, the bottom of the upper subband rises above the Fermi level around 4.2 T, marking the onset of subband depopulation and consistent with the experiment of Sec. II B. This is a direct consequence of the increase in the subband density of states resulting from the electron effective mass renormalization, i.e., the change in the dispersion relation curvature. This renormalization is more pronounced in the case of the WQW upper subband than for the NQW ($1.36m^*$ and $1.05m^*$ at $B=6$ T, respectively).

Comparing the two subbands in the WQW, $E_C(k_x)$ for the upper band keeps a parabolic shape even at high fields ($B=6$ T) as opposed to the curvature of the lower subband, which strongly varies with increasing parallel B. More precisely, the local energy minimum observed at $B=0$ splits into a local maximum and two local minima as the parallel B is increased.

To give a more visual understanding of the effect of a parallel B on the conduction band properties of the narrow and wide QWs, we now discuss the Fermi contours. Figure 13 shows the self-consistently calculated Fermi lines with increasing B of the NQW ground state (a), lower (b), and upper (c) WQW subbands. In both dots, the $B=0$ perfectly circular contours get slowly deformed as the parallel B is increased. In the case of the NQW, the distortion of the Fermi line is very limited. On the contrary, both the upper and lower subband contours in the WQW are strongly dis-

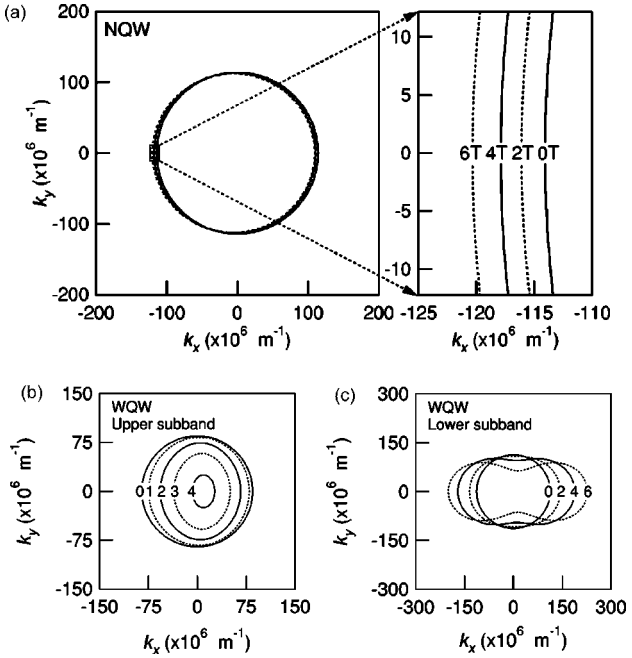

FIG. 13. Self-consistent Fermi lines at indicated values of the magnetic field B and for (a) the ground state of the NQW, (b) the upper, and (c) lower occupied subbands of the WQW sample. The right panel in (a) is a closeup of the Fermi lines in the small window indicated on the left panel. In (b), the range of investigated B's is limited to 4 T, as the subband is fully depleted for $B>4.2$ T.

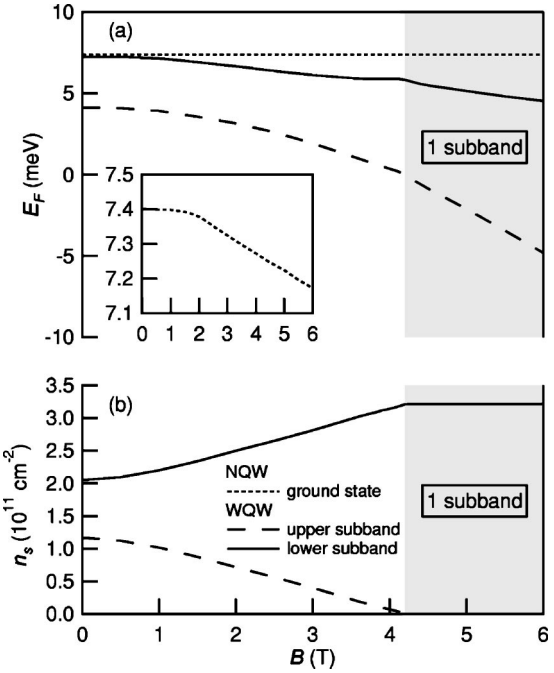

FIG. 14. (a) Self-consistent calculation of the variation of E_F with B for the ground state of the NQW and for the two occupied subbands of the WQW. Here E_F is calculated with respect to the corresponding conduction band edges. Inset: The calculated $E_F(B)$ in the NQW. (b) Calculated sheet densities n_s of the lower and upper occupied subbands in the WQW with increasing magnetic field B. The total density is 3.2×10^{11} cm^{-2}. The gray regions indicate the B range where only one subband is occupied in the WQW sample.

torted. While the lower subband contour takes a "peanut"-like shape, the ellipsoidal surface enclosed by the upper subband contour decreases with increasing B and disappears above 4 T.

It is clear from the Fermi contours of Fig. 13, that there are fundamental differences in the variation of the Fermi level with respect to the bottom of the occupied subbands in our samples. Because transport in the open dots occurs through electrons with energies close to E_F, this also means that trajectories in the dots, located in reciprocal space around the Fermi contours, will be more strongly affected by the parallel B in the WQW dot. Figure 14(a) shows E_F as a function of B for the three indicated subbands. Numerically, $E_F(B)=-E_C(B,k_x=k_{min})$, where k_{min} is the location of the subband minimum at a given B in the dispersion relations of Figs. 11 and 12. In the case of the NQW, the variation of E_F with B is small [0.2 meV, see the inset to Fig. 14(a)] compared with the 3 and 9 meV values calculated for the lower and upper subbands in the WQW, respectively. Another interesting feature in Fig. 14(a) is the subband depopulation that occurs around 4.2 T, consistent with the value of B where the sudden drop in transverse magnetoresistance is observed in the inset to Fig. 6(b). The gray region in the figure indicates that only one subband is occupied [the Fermi level of the upper band (dashed curve) has negative values]. The upper band depopulation in the WQW is even more visible in Fig. 14(b) at the electron sheet densities contributed by the lower (plain curve) and upper (dashed curve) subbands. As B increases, electrons are slowly transfered from the upper to lower band, while the total sheet density remains constant.

V. E_F-INDUCED MCFs

We now discuss the experimental results of Sec. II in light of the self-consistent simulations of Sec. IV. The presence of MCFs under a strictly parallel B can be linked to the non-negligible changes in the position of E_F with respect to the conduction band edge as B increases. This variation of $E_F(B)$, particularly large in the case of the WQW, is similar to the variation of the Fermi level obtained by sweeping the voltage on electrostatic gates.[49]

It is therefore relevant to present the $\theta=90°$ magnetoconductances of Fig. 9 in terms of energy instead of the magnetic field. The idea is to obtain a mapping between B and the variation δE_F of the Fermi level with respect to the conduction subband edges in the QWs. Because only a single band is occupied by electrons in the NQW sample, δE_F can be readily calculated using the $E_F(B)$ curve in Fig. 14(a),

$$\delta E_F(B) = \left|E_F(B) - E_F(B=0)\right|. \tag{14}$$

Unfortunately, this relation is not directly applicable to the WQW as two subbands contribute to transport in the dot, at least until the onset of subband depopulation is reached. As a result, the two $E_F(B)$ curves of Fig. 14(a) for the WQW upper and lower subbands must be combined here in a meaningful way to obtain a single $\delta E_F(B)$ relation. For this purpose, we propose the following empirical arguments: (1) Macroscopically, it is reasonable to consider that the average

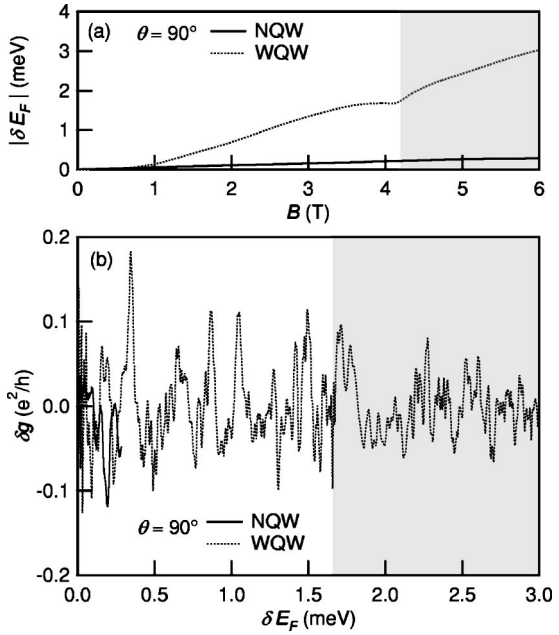

FIG. 15. (a) Variation with magnetic field B of the self-consistent effective Fermi energy δE_F in the narrow (plain curve) and wide (dotted curve) quantum wells. For the WQW, the two $E_F(B)$ relations for the upper and lower occupied subbands shown in Fig. 14(a) were merged into a single $\delta E_F(B)$ using Eq. (15). MCFs of the narrow and wide quantum wells as a function of δE_F. The gray region indicates the energy range where only one subband is occupied in the WQW sample.

magnetoconductance $\langle g \rangle$ across the dot at $\theta = 90°$ is a good image of δE_F. This is supported by the fact that $\langle g \rangle$ is strongly influenced by the transfer of electrons from the upper to the lower subband as B increases. In particular, when the upper band is fully depleted, $\langle g \rangle$ remains constant. (2) At lower magnetic fields, a sensible hypothesis would be that the contributions to δE_F of the two occupied subbands are proportional to their respective weights in the total sheet density n_s. (3) Finally, because the MCFs are created by the variation of E_F with B and do not depend on its absolute value at a given field, it seems reasonable to extract δE_F from a density weighted average of first order derivatives of $E_F(B)$ for the two occupied subbands. Based on these arguments, we propose

$$\delta E_F(B) = \left| \int_0^B \left(\frac{\partial E_F^{up}(B')}{\partial B'} \frac{n_s^{up}(B')}{n_s(B')} + \frac{\partial E_F^{low}(B')}{\partial B'} \frac{n_s^{low}(B')}{n_s(B')} \right) dB' \right| \tag{15}$$

for the WQW, where $n_s^{up}(B)$, $n_s^{low}(B)$, and $n_s(B) = n_s^{up}(B) + n_s^{low}(B)$ are the upper subband, lower subband, and total sheet densities at a given B, respectively. Here E_F^{up} and E_F^{low} are the positions of the Fermi level with respect to the bottom of the upper and lower subbands, as represented in Fig. 14(a).

Figure 15(a) shows the calculated δE_F obtained from Eqs. (14) and (15) for the narrow and wide quantum well under a strictly parallel B. The difference in energy variation between the two wells is striking. The onset of subband depopulation in the WQW is clearly marked by a kink in δE_F. The gray region corresponds to the range of magnetic fields where only one subband is populated in the WQW. We next use the mapping relation between B and δE_F illustrated in Fig. 15(a) to rescale the $\theta = 90°$ magnetoconductance curves of Fig. 9 [panels (b) and (d)]. Figure 15(b) shows the MCFs in the full energy range (from 0 to 3.0 meV) covered by E_F in the WQW dot. By rescaling B into δE_F, it becomes apparent that the parallel magnetic field probes only a small subset of MCFs in the NQW dot compared to what happens with the WQW dot. Moreover, the energy-scaled fluctuations have similar periodicities, meaning that δE_F is indeed the ruling parameter. This observation reinforces our interpretation that these MCFs have their origin in the probing of electron trajectories in the dot by the Fermi level, with a strength that depends on the well width and on the parallel B-induced orbital effect.

In Sec. III a frequency analysis of the MCFs in tilted magnetic fields was performed and an effective tilt angle θ_{B_c} was extracted from the power spectrum of $\delta g(B)$. It was found that θ_{B_c} saturates as $\theta \to 90°$. As discussed earlier in the text, it seems more appropriate in the case of the $\theta = 90°$ MCFs to perform a power spectrum analysis in energy space, using the $B \to \delta E_F$ mapping of Fig. 15(a). Because the $\theta = 90°$ MCFs spectrum in the NQW dot has a limited frequency distribution, we restrict our analysis to the $\delta g(\delta E_F)$ conductance obtained in the WQW dot [Fig. 15(b), dotted curve]. An average power spectrum in energy space $S_E(f_E)$ is calculated using the same procedure as in Sec. III for the power spectrum $S_B(f_B)$ in magnetic field space. Similar to the result of Eq. (2), the MCFs' autocorrelation function in energy space is a Lorentzian[50] and yields an exponentially decreasing power spectrum density,

$$S_E(f_E) = S_E(0) e^{-2\pi E_S f_E}, \tag{16}$$

where E_S is a characteristic energy.

Figure 16 shows power spectra in energy space of the WQW dot MCFs $\delta g(\delta E_F)$ at $\theta = 90°$. A good agreement between the experimental $S_E(f_E)$ and the theoretical prediction of Eq. (16) is obtained by evaluating and fitting the power spectrum on two distinct domains, delimited by the onset of subband depopulation in the WQW. The two domains are those depicted in Fig. 15 and correspond to $0 < \delta E_F < 1.7$ meV and $1.7 < \delta E_F < 3$ meV. On Fig. 16, the set of red curves represents the power spectrum and the fit to the dotted curve of Fig. 15(b) for $0 < \delta E_F < 1.7$ meV, where two subbands are occupied. The blue curves were obtained in the energy domain $1.7 < \delta E_F < 3$ meV, where the upper subband is fully depleted. The calculated characteristic energies E_S are 0.010 and 0.013 meV for the one and two occupied subbands configurations, respectively. Interestingly, this increase of E_S with the number of occupied subbands is expected as the semiclassical theory predicts[54] that $E_S \propto N\Delta/\pi$. As Δ remains constant, the only parameter that can influence the value of E_S for parallel B-induced MCFs is the number of transmission modes. The drop in the background magnetoconductance and the drop around 4.2 T, observed when the

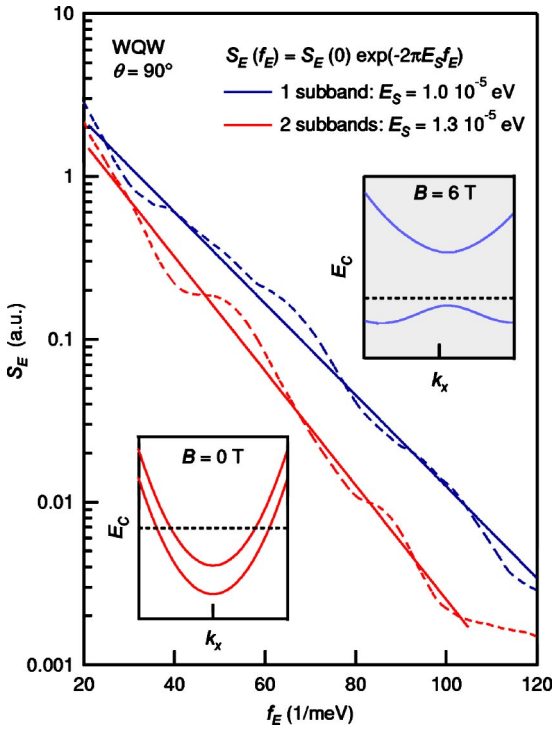

FIG. 16. (Color online) Frequency analysis as a function of energy of the WQW dot MCFs. Here $\delta g(\delta E_F)$ is Fourier transformed on the selected energy ranges (see the text) to obtain the average power spectra S_E shown in the figure as dashed red and blue curves. The plain red and blue curves are one-parameter fits (see the text) to these $S_E(f_E)$ spectra. Insets: Dispersion relations of the wide quantum well at $B=0$ [$\delta g(E_F)=0$, two occupied subbands, lower panel] and $B=6$ T [$\delta g(E_F)=3$ meV, one occupied subband, upper panel]. The position of the Fermi level is indicated as a dotted line.

WQW dot is subject to a parallel field (Fig. 6), is an image of the reduction of N as the upper subband gets depopulated and does not contribute anymore to the transmission modes into the dot. Using an effective radius of 0.75 μm for the dot, which takes into account the depletion region induced by the sample wet etching, the mean-level spacing is 4×10^{-3} meV. Further, assuming that N is reduced from 10 to 8 as the magnetoconductance g decreases from 5 to $4e^2/h$ because of subband depopulation, the theoretical value of E_S is expected to drop from 0.0128 to 0.0102 meV, which is clearly in good agreement with the values of E_s extracted from the experimental power spectra.

VI. CONCLUSIONS

In this work we have investigated magnetoconductance fluctuations (MCFs) generated in ballistic quantum dots in tilted magnetic fields. Using two (NQW and WQW) samples, we compared the magnetotransport properties of the quantum dots as a function of the well width and the tilt angle. We observed strong similarities in the temperature dependence of the perpendicular and parallel B-induced MCFs. The differences between the rich spectrum of parallel B-induced MCFs in the WQW dot and the MCFs measured in the NQW dot were analyzed by means of an effective tilt angle θ_{B_c}, extracted from the power spectra of the magnetoconductance curves. It was found that θ_{B_c} saturates as $\theta\rightarrow90°$. The strong dependence of this saturation angle on the well width confirms that the interplay between the electrostatic and magnetic confinements of the 2DEG is the source of the parallel B-induced MCFs. Self-consistent Poisson-Schrödinger simulations indicate that a parallel B has a very different effect on the subbands dispersion relations and Fermi contours of the NQW and WQW samples. Likewise, the position of E_F does not vary significantly in the NQW with increasing B. On the contrary, in the WQW the strong variation of E_F is related to the electron depopulation of the upper subband. A remapping of B into a self-consistently calculated effective Fermi energy δE_F revealed that the parallel magnetic field probes only a limited set of MCFs in the NQW dot compared to the WQW sample. Furthermore, a good agreement was found between the power spectrum analysis in energy space of the WQW magnetoconductance at $\theta=90°$ and theory. This is a confirmation of the relevance of the δE_F rescaling for the interpretation of parallel B-induced MCFs.

ACKNOWLEDGMENTS

We thank M. Verstraete for stimulating discussions. We also acknowledge the effort of M. B. Santos, who grew the MBE samples. This work is supported by an ARO grant, NSF, and the von Humboldt Foundation (Princeton), F.R.I.A. and F.N.R.S. (Louvain-la-Neuve).

*Electronic address: gustin@pcpm.ucl.ac.be

[1] C. M. Marcus, A. J. Rimberg, R. M. Westervelt, P. F. Hopkins, and A. C. Gossard, Phys. Rev. Lett. **69**, 506 (1992).
[2] A. G. Huibers, S. R. Patel, C. M. Marcus, P. W. Brouwer, C. I. Duruoz, and J. S. Harris, Phys. Rev. Lett. **81**, 1917 (1998).
[3] R. P. Taylor, R. Newbury, A. S. Sachrajda, Y. Feng, P. T. Coleridge, C. Dettmann, N. Zhu, H. Guo, A. Delage, P. J. Kelly, and Z. Wasilewski, Phys. Rev. Lett. **78**, 1952 (1997).
[4] D. K. Ferry, R. Akis, and J. P. Bird, Phys. Rev. Lett. **93**, 026803 (2004).
[5] R. Ketzmerick, Phys. Rev. B **54**, 10 841 (1996).
[6] A. P. S. de Moura, Y. C. Lai, R. Akis, J. P. Bird, and D. K. Ferry, Phys. Rev. Lett. **88**, 236804 (2002).
[7] C. W. J. Beenakker, Rev. Mod. Phys. **69**, 731 (1997).
[8] J. A. Folk, S. R. Patel, K. M. Birnbaum, C. M. Marcus, C. I. Duruoz, and J. S. Harris, Phys. Rev. Lett. **86**, 2102 (2001).
[9] B. I. Halperin, A. Stern, Y. Oreg, J. N. H. J. Cremers, J. A. Folk, and C. M. Marcus, Phys. Rev. Lett. **86**, 2106 (2001).
[10] I. L. Aleiner and V. I. Fal'ko, Phys. Rev. Lett. **87**, 256801 (2001).
[11] P. W. Brouwer, J. N. H. J. Cremers, and B. I. Halperin, Phys. Rev.

B **65**, 081302(R) (2002).
[12] J. S. Meyer, A. Altland, and B. L. Altshuler, Phys. Rev. Lett. **89**, 206601 (2002).
[13] V. I. Fal'ko and T. Jungwirth, Phys. Rev. B **65**, 081306(R) (2002).
[14] J. H. Cremers, P. W. Brouwer, and V. I. Fal'ko, Phys. Rev. B **68**, 125329 (2003).
[15] D. M. Zumbuhl, J. B. Miller, C. M. Marcus, V. I. Fal'ko, T. Jungwirth, and J. S. Harris, Phys. Rev. B **69**, 121305(R) (2004).
[16] C. Gustin, S. Faniel, B. Hackens, S. Melinte, M. Shayegan, and V. Bayot, Phys. Rev. B **68**, 241305(R) (2003).
[17] Y. W. Suen, J. Jo, M. B. Santos, L. W. Engel, S. W. Hwang, and M. Shayegan, Phys. Rev. B **44**, 5947 (1991).
[18] T. S. Lay, T. Jungwirth, L. Smrcka, and M. Shayegan, Phys. Rev. B **56**, R7092 (1997).
[19] T. M. Fromhold, L. Eaves, F. W. Sheard, M. L. Leadbeater, T. J. Foster, and P. C. Main, Phys. Rev. Lett. **72**, 2608 (1994).
[20] T. M. Fromhold, P. B. Wilkinson, F. W. Sheard, L. Eaves, J. Miao, and G. Edwards, Phys. Rev. Lett. **75**, 1142 (1995).
[21] T. Jungwirth and L. Smrcka, J. Phys.: Condens. Matter **5**, L217 (1993).
[22] J. M. Heisz and E. Zaremba, Phys. Rev. B **53**, 13 594 (1996).
[23] R. A. Jalabert, H. U. Baranger, and A. D. Stone, Phys. Rev. Lett. **65**, 2442 (1990).
[24] J. Spector, H. L. Stormer, K. W. Baldwin, L. N. Pfeiffer, and K. W. West, Appl. Phys. Lett. **56**, 1290 (1990).
[25] H. Van Houten, B. J. Van Wees, J. E. Mooij, C. W. J. Beenakker, J. G. Williamson, and C. T. Foxon, Europhys. Lett. **5**, 721 (1988).
[26] B. Hackens, F. Delfosse, S. Faniel, C. Gustin, H. Boutry, X. Wallart, S. Bollaert, A. Cappy, and V. Bayot, Phys. Rev. B **66**, 241305(R) (2002).
[27] J. Heremans, B. K. Fuller, C. M. Thrush, and D. L. Partin, Phys. Rev. B **52**, 5767 (1995).
[28] R. M. Clarke, I. H. Chan, C. M. Marcus, C. I. Duruoz, J. S. Harris, K. Campman, and A. C. Gossard, Phys. Rev. B **52**, 2656 (1995).
[29] K. Frahm, Europhys. Lett. **30**, 457 (1995).
[30] A. G. Huibers, M. Switkes, C. M. Marcus, K. Campman, and A. C. Gossard, Phys. Rev. Lett. **81**, 200 (1998).
[31] D. P. Pivin, A. Andresen, J. P. Bird, and D. K. Ferry, Phys. Rev. Lett. **82**, 4687 (1999).
[32] M. Buttiker, Phys. Rev. B **33**, 3020 (1986).
[33] A. Yacoby, M. Heiblum, H. Shtrikman, V. Umansky, and D. Mahalu, Semicond. Sci. Technol. **9**, 907 (1994).
[34] U. Sivan, Y. Imry, and A. G. Aronov, Europhys. Lett. **28**, 115 (1994).
[35] T. Englert, J. C. Maan, D. C. Tsui, and A. C. Gossard, Solid State Commun. **45**, 989 (1983).
[36] G. Salis, T. Heinzel, K. Ensslin, O. J. Homan, W. Bachtold, K. Maranowski, and A. C. Gossard, Phys. Rev. B **60**, 7756 (1999).
[37] M. Shayegan, T. Sajoto, M. Santos, and C. Silvestre, Appl. Phys. Lett. **53**, 791 (1988).
[38] I. H. Chan, R. M. Clarke, C. M. Marcus, K. Campman, and A. C. Gossard, Phys. Rev. Lett. **74**, 3876 (1995).
[39] H. A. Weidenmuller, Physica A **167**, 28 (1990).
[40] F. Stern and W. E. Howard, Phys. Rev. **163**, 816 (1967).
[41] S. Nagaraja, P. Matagne, V. Y. Thean, J. P. Leburton, Y. H. Kim, and R. M. Martin, Phys. Rev. B **56**, 15 752 (1997).
[42] J. M. Heisz and E. Zaremba, Semicond. Sci. Technol. **8**, 575 (1993).
[43] L. Smrcka and T. Jungwirth, J. Phys.: Condens. Matter **7**, 3721 (1995).
[44] J. P. Perdew and A. Zunger, Phys. Rev. B **23**, 5048 (1981).
[45] D. M. Ceperley and B. J. Alder, Phys. Rev. Lett. **45**, 566 (1980).
[46] C. M. Wolfe, N. Holonyak, and G. E. Stillman, *Physical Properties of Semiconductors* (Prentice-Hall, Englewood Cliffs, NJ, 1989).
[47] C. D. Simserides, J. Phys.: Condens. Matter **11**, 5131 (1999).
[48] T. Ando, J. Phys. Soc. Jpn. **54**, 1528 (1985).
[49] M. W. Keller, O. Millo, A. Mittal, D. E. Prober, and R. N. Sacks, Surf. Sci. **305**, 501 (1994).
[50] K. Efetov, *Supersymmetry in Disorder and Chaos* (Cambridge University Press, Cambridge, England, 1997).
[51] J. P. Lu and M. Shayegan, Phys. Rev. B **58**, 1138 (1998).
[52] The assumption that the mobility is identical for the two occupied subbands in the WQW might not be totally justified (Ref. 51). However, a precise evaluation of the mean free path is not critical to the discussion as long as it is larger than the dot dimensions, which is obviously the case in our samples.
[53] Under a strictly parallel field, the transverse magnetoresistance should be identically zero. We attribute the quasiparabolic variation of ΔR shown in the inset to Fig. 3(b) to a small, unaccounted for longitudinal component of the resistance coming from a small geometrical imperfection of the Hall bar pattern.
[54] The same expression for E_S can also be obtained through Ref. 50 as semiclassical approximations (Ref. 23) and the methods in Ref. 50 give the same expressions for the MCFs autocorrelation function in both magnetic field and energy spaces.